

Article

Impact of Domain Nesting on High-Resolution Forecasts of Solar Conditions in Central and Eastern Europe

Michał Mierzwiaik *  and Krzysztof Kroszczyński 

Faculty of Civil Engineering and Geodesy, Military University of Technology, Gen. S. Kaliskiego 2, 00-908 Warsaw, Poland; krzysztof.kroszczyński@wat.edu.pl

* Correspondence: michal.mierzwiaik@wat.edu.pl

Abstract: The article presents a study on the impact of the domain nesting method on the results of simulated solar conditions using the mesoscale Weather Research and Forecasting model. The analysis included 8 consecutive days (July 2022), which were characterized by cloudless conditions, as well as complex situations related to the passing of a cold front. The study covered a region located in Central and Eastern Europe—the southern area of eastern Germany. The results of the model simulations using the adopted domain configurations (with spatial resolutions of 9, 3, and 1 km; 3 and 1 km; and 5 and 1 km) were compared to data from ground measurements from Deutscher Wetterdienst (DWD) stations. The effect of the duration of the triggered prediction on the quality of the output data was also investigated, and for this purpose, short-term predictions covering 24 and 48 h, respectively, were selected. Research revealed the advantages of one combination of domains—3 and 1 km—over the others and showed that the results of simulations with different duration lengths were characterized by consistent results. Research supports the demand for high-quality forecasts of solar conditions, which are extremely important in the process of managing energy systems.

Keywords: solar radiation; renewable energy sources; solar energy; WRF; cold fronts



Citation: Mierzwiaik, M.; Kroszczyński, K. Impact of Domain Nesting on High-Resolution Forecasts of Solar Conditions in Central and Eastern Europe. *Energies* **2023**, *16*, 4969. <https://doi.org/10.3390/en16134969>

Academic Editor: Jesús Polo

Received: 17 May 2023

Revised: 20 June 2023

Accepted: 22 June 2023

Published: 26 June 2023



Copyright: © 2023 by the authors. Licensee MDPI, Basel, Switzerland. This article is an open access article distributed under the terms and conditions of the Creative Commons Attribution (CC BY) license (<https://creativecommons.org/licenses/by/4.0/>).

1. Introduction

The role of renewable energy sources (RES; Table A1 includes a description of abbreviations used) is steadily growing. Once regarded as a futuristic invention, today they are one of the main alternatives to conventional energy sources. The European Union's (EU) policy is to further increase the share of energy gained from renewable sources in order to become as independent from fossil fuels as possible in the near future [1,2]. RES allow greater independence and security in the field of crisis management, which includes strategic branches of the economy to which the energy sector belongs. Among the possible RES, solar energy has the greatest potential. The possibilities offered, above all, by photovoltaic (PV) installations make them the most frequently chosen RES solutions. Technological progress makes PV installations ever-more efficient and, importantly, ever-more affordable [3]. These types of installations can be configured in any way one likes, ranging from small backyard sites to large-scale solar farms. Panels of different sizes and parameters are available, which can be mounted on different surfaces, i.e., stationary, as well as mobile, objects. The use of slightly more advanced solutions (tracking systems) makes it possible to make optimal use of the solar radiation reaching a given part of the earth and its conversion into electricity (PV installations) or heat (solar thermal collectors) [2]. In the case of energy from the sun, in addition to latitude (which determines the most important factor—the angle of incidence of the sun's rays), weather conditions play a key role. Properly located PV modules (proper orientation, tilt, no shading effect, etc. [4]), in the case of significant cloud cover occurring, will not be able to generate the expected amount of energy. The region of Central and Eastern Europe (CEE) is not characterized by the best solar conditions, while

the efficient use of solar radiation reaching the Earth's surface could significantly improve the operation of the energy sectors of countries in the region. In the current situation of growing demand for electricity, each additional source of energy is extremely important, particularly those that do not involve greenhouse gas emissions (especially CO₂) [5,6]. Due to the still-growing number of photovoltaic installations, the management of electricity resources is becoming an increasing problem. This issue is especially noticeable during the summer season, when, under favorable weather conditions (high, cloudless weather), the amount of energy generated by the solar RES sector increases rapidly. One solution that could improve the management of the energy system includes the use of numerical weather forecast models that take into account the forecasting of solar conditions from Numerical Weather Prediction model—NWP [7] (e.g., Weather Research and Forecasting Model (WRF-Solar [8])). Short-term predictions (up to 72 h) of meteorological elements are characterized by high verifiability [9,10]. This issue makes their use (especially in solar parameters) potentially indispensable, especially due to the further dynamic development of this RES sector. The share of solar energy integrated into the power grid is increasing year by year [11]. In the case of Germany, the capacity of installations during the five-year period 2014–2019 increased from 38,301 to 49,016 [W·10⁶], while in Poland, this change was much greater: from 24 to 1317 [W·10⁶]. In Austria, solar installations' capacity grew from 770 to 1660 [W·10⁶]. In the Czech Republic, the largest growth in the solar sector took place between 2008 and 2013, when total capacity grew from 55 to 2064 [W·10⁶] [11]. This trend has been going on for more than a dozen years, and there is no indication that the situation is going to change, either in the near or more distant future. The EU prioritizes efforts to improve the energy security of its member countries, as well as to contribute to a significant reduction in the use of conventional energy sources. This shift will improve the natural environment and help reduce the impact of member countries on progressive climate change. The EU, since the early 1990s, has supported the development of renewable energy sources, contributing to the reduction in greenhouse gas emissions, while increasing energy security in the community. Current actions aim to reduce CO₂ emissions by 40% by 2030 compared to 1990, while the share of energy from renewable sources is expected to reach 27% [12–15].

Due to the constantly increasing share of electricity obtained from renewable energy sources (RES), especially from photovoltaic installations in the CEE region (as well as the rest of Europe and beyond), it is becoming more important to forecast the amount of energy generated in this way. Currently, the best way to simulate future energy yield (especially for short-term forecasts) is to use NWPs [16–20]. They enable us to predict various meteorological elements, including solar parameters, for different time horizons (short, medium, and long term forecasts). The greatest verifiability is characterized by forecasts covering shorter time intervals, i.e., the short and medium term (up to 7 days) [21,22]. Predictions developed for spatially limited areas, taking into account their specifics (natural conditions), also have better verifiability relative to forecasts for vast, highly diverse areas. One of the biggest challenges in the forecasting of atmospheric conditions is the parameterization of the numerical weather forecast model. Due to the multiplicity of factors affecting the forecast, to achieve optimal results, one should take into account the specific features of the natural environment of a given area (such as the terrain of the Earth's surface, land cover, water network, etc.) [23–26]. In the case of forecasts of solar conditions, the aforementioned aspects are extremely important—they condition, among other things, the formation of cloudiness of a local character (related to the proximity of forested areas [27] or the influence of urban areas [28]), which is one of the most significant elements affecting the amount of direct solar radiation reaching the Earth's surface. The above arguments clearly support the development of forecasts dedicated to spatially limited areas, which will take into account the local characteristics of the environment [29–31].

The aim of the present study was to evaluate the effect of the way domains are nested in the WRF model on the results obtained from direct solar radiation forecasts. In addition, we aim to compare the results of 24- and 48-h simulations. The size of the

area for which future atmospheric conditions are simulated is important in terms of the quality of forecasts, as well as for technical reasons—the selection of the right size and spatial resolution of domains affects the duration of the simulation and optimization of the process of its acquisition (appropriate use of computing power, including by selecting the appropriate number of grid nodes in the domains, reducing the duration of the simulation, etc.) [32–34]. We decided to study the effect of the grid parent ratio used on the results of WRF model forecasts for a specific area located in the CEE region that covers the southern part of eastern Germany. The area encompassing the southern part of eastern Germany was chosen as being representative of Central and Eastern Europe, which, in turn, is of interest (research) to us due to the presence of different types of relief, altitude, or land cover. In addition, data are available for the region from direct measurements made at DWD stations, which represent a more dense, evenly distributed measurement network compared to neighboring countries. However, the region is also characterized by varying relief, water conditions, etc., which makes forecasting the amount of solar radiation, even for such a small area, rather complex.

This article is intended to indicate the optimal means of nesting domains (the appropriate grid-parent ratio) for analyses carried out in the CEE region for solar conditions. The default WRF-Solar model configuration used in the study assumes the use of shallow-convection parameterization (Deng scheme) [35,36] and the deactivation of cumulus parameterization. The Deng scheme allows activation of the effect of unresolved clouds on shortwave radiation (the shallow cumulus scheme also accounts for deep convection). Studies such as [37], among others, have shown that the use of different cumulus parameterizations yields the best results for domains with the largest resolutions (e.g., 3 km, 1 km). Although best practices suggest excluding cumulus parameterizations for domains smaller than 4 km [38], shallow-cumulus parameterization (Deng scheme) is used instead in WRF-Solar. In the case of the present study, the domains with the highest level of spatial resolution (1 km) had high agreement with the observed data (which are best seen in the context of high-pressure situations).

In many studies related to the modeling of atmospheric conditions, including meteorological elements directly related to cloud cover (convective phenomena, precipitation, thunderstorms, tornadoes, lightning, etc.) have been used, with sequence of domains 9 km, 3 km, 1 km [34,35,39–44], which we also implemented. This method is one of the most widely used domain nesting schemes. Other authors also carried out studies using the WRF-Solar model, where only a domain with a spatial resolution of 9 km [45] or 9 km and 3 km [46] was used. For example, a forecast of heavy rainfall was analyzed using the WRF model for the Korean Peninsula area, which used domains with spatial resolutions equal to 5 km and 1 km [47], while another study used the sensitivity of intense rainfall to domain size, in which experiments were carried out on a domain with a resolution of 9 km and 5 km [48]. All of the above-mentioned studies used domains that fall within the gray zone. In addition, in [49], among others, a positive effect of cumulus parameterization on the ability to forecast precipitation was demonstrated (in the case of the 8 km resolution domain, among others). In [50], the authors conducted tests using various cumulus parameterization schemes to determine their capabilities in forecasting rainfall in Southeast Asia with the use of high spatial resolutions. In [51], it was shown that the application of Deng's shallow convection scheme [35] for grids with a resolution of 9 km exhibits a clear similarity of course with respect to the WRF-LES (large-eddy simulations) parameterization. The authors suggest that for higher resolutions, the waveform will be even more similar to the reference values (WRF-LES). Also, they indicated that shallow convection parameterization may predict variables, such as domain-averaged shortwave radiation, correctly.

The research is a case study to develop an optimal domain nesting scheme in the context of further work on short-term forecasts of solar conditions in the CEE region. The purpose of the article is to identify the best of the commonly used methods of (domain) nesting (grids) for the area under consideration, taking into account various atmospheric conditions.

2. Materials and Methods

The area under study covers the southern part of eastern Germany and is part of Brandenburg and Saxony. The region is located at a latitude between 50.4 and 52.1° degrees north and at a longitude between 11.6 and 14.3° degrees east. The area consists of two predominant types of relief: lowlands in the north (forming part of the Central German Lowlands) and the foothills of the Ore Mountains in the south (Figure 1).

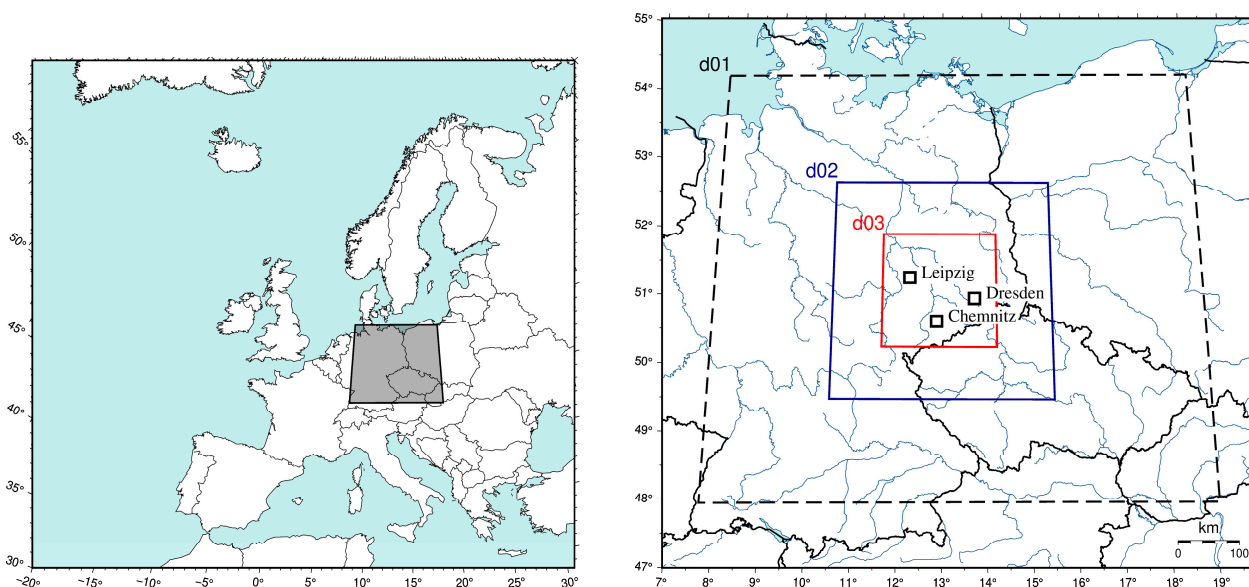


Figure 1. The location of the analyzed area (on the left) and the location of the Deutscher Wetterdienst (DWD) stations (illustration on the right). Domains d03 and d02 are identical for the configuration with grid parent ratio 3 (in the case of a two-domain combination, they are d01 and d02, respectively). For the CR_5_2D configuration, the domain areas coincide with the domains shown in the attached map: d02 = d01 and d03 = d02.

In an effort to verify the data obtained from the WRF model simulations, they were compared to direct measurements from three meteorological stations operating within the Deutscher Wetterdienst (DWD) that perform actinometric measurements: Chemnitz, Dresden–Klotzsche, and Leipzig–Halle [52]. Data from direct measurements made via DWD stations represented hourly sums of solar radiation reaching the Earth’s surface. In the case of the WRF model—hourly sums of shortwave surface downward direct irradiance—SWDDIR parameter values were also generated. To compare data from direct measurements with model data, bilinear interpolation was used to extract specific points.

Characteristics of the stations—geographical coordinates and height above sea level—can be found in Table 1.

Table 1. Characteristics of DWD stations.

Station Name	Station_id	Geographical Coordinates		Height above Sea Level (m)
		N	E	
Leipzig/Halle *	2932	51.4347	12.2396	131
Dresden/Klotzsche *	1048	51.1278	13.7543	227
Chemnitz	853	50.7913	12.8720	416

* The names of the Leipzig/Halle and Dresden/Klotzsche stations will be used in the article hereafter in abbreviated form, respectively, as Leipzig and Dresden.

To compare the results obtained with the values measured at DWD stations, the following statistics were used: root mean square error (RMSE) (1), mean absolute error (MAE) (2), and mean bias error (MBE) (3):

$$\text{RMSE} = \sqrt{\frac{\sum_{i=1}^N (\text{model data(WRF)}_i - \text{measured data(DWD)}_i)^2}{N}} \quad (1)$$

$$\text{MAE} = \frac{1}{N} \sum_{i=1}^N |\text{model data(WRF)}_i - \text{measured data(DWD)}_i| \quad (2)$$

$$\text{MBE} = \frac{1}{N} \sum_{i=1}^N (\text{model data(WRF)}_i - \text{measured data(DWD)}_i) \quad (3)$$

In addition to the most commonly used statistics, the Nash–Sutcliffe Efficiency (NSE) coefficient [53,54] was also used to compare the results of weather forecasts obtained from NWP [19,55,56].

$$\text{NSE} = 1 - \frac{\sum_{i=1}^N (\text{measured data(DWD)}_i - \text{model data(WRF)}_i)^2}{\sum_{i=1}^N \left(\text{measured data(DWD)}_i - \overline{\text{measured data(DWD)}} \right)^2} \quad (4)$$

The RMSE is one of the most widely used statistical indicators (among other things, it is used to assess the effectiveness of models), with its characteristic being that it assigns higher weights to errors with larger values. Additionally, nRMSE normalized by the average value from the direct measurements was used to aggregate data summaries. The MAE coefficient was used to describe the mean error and the distribution of its values, and the MBE indicates the mean value of the model's error and determines whether the values obtained by the model are overestimated or underestimated relative to the reference data [57–59]. The NSE coefficient, like the RMSE, should not be used alone; thus, it was decided to use both. The preferred values of NSE were close to one; negative values indicate inadequate quality of results, which, in this case, referred to the forecasts of meteorological elements [53,54]. The choice of both RMSE and NSE coefficients allowed us to evaluate simulation results (the limitations of each coefficient are balanced).

The boundary and initial conditions interpolated to the mesoscale WRF model grids were taken from the Global Forecast System (GFS). In practice, two divisions of the GFS model master grid are usually used (quarter-degree resolution and linear mesh size were ~27 km). In the first case, the linear grid sizes of the mesoscale model grid were obtained by using a 3 subdivision, whereas in the second case, a 5 subdivision was used [60,61]. Consequently, grids of 3 km, 1 km, 5 km, etc. can be used. As can be seen, the first division shows grids with higher spatial resolution. However, this result may be at the cost of the quality of interpolation of the ties of these grids obtained from the GFS master model data. Higher resolution downscaling enabled better simulation results, as well as a more complete understanding of the impact of environmental elements on specific meteorological elements [62,63]. The most commonly chosen domain configuration for analysis or prediction of meteorological elements, as well as extreme phenomena, is triple nested with a grid parent ratio of 3 (usually with the following spatial resolution of the individual grids: 9 km, 3 km, and 1 km [34,39–42]). For the WRF model, two values of grid parent ratio were recommended: 3 and 5 [60,61]. Many of the studies conducted so far showed the superiority of using grids with a spatial resolution of 4 km and higher [64–66], which allowed authors to obtain better results. The above solutions have a particularly important impact on the prediction of meteorological elements or phenomena directly or indirectly related to cloud cover (cloud cover, rainfall, snowfall, solar radiation, etc.) [40–42,64,66,67]. Designing the optimal domain and selecting the appropriate model parameterization and forecast duration allowed us to obtain the desired forecast quality of a specific element or group of meteorological elements [23,66,68].

In Section 3, for the selected term, the data obtained from simulations and direct measurements were compared with the potential (R_{pot}) values (direct component of radiation to the horizontal plane), which were determined according to the following Formula (5) [68–70]:

$$R_{pot} = I_0 \cdot [\cos\varphi \cdot \cos H \cdot \cos\delta + \sin\varphi \cdot \sin\delta] \quad (5)$$

where I_0 is the solar constant ($1368 \text{ [W} \cdot \text{m}^{-2}]$) which was taken from [71]; φ is the latitude; H is the hour angle; and δ is the sun's declination. The value of potential radiation was determined for each hour (in which direct radiation reached the Earth's surface).

2.1. Synoptic Situations

The study covered a period of eight days: 17–24 July 2022. The selected time interval was associated with high-pressure situations, which further provide an opportunity to compare forecasts with measured data and relate them to direct components of radiation in the horizontal plane values. In addition, a wavy cold front moved over the region during the selected period, which was a difficult process for numerical models to simulate [72]. The front was also accompanied by a line of convergence, which further complicated the ability of numerical weather prediction models to predict atmospheric conditions. For the above reasons, the selected period provided a representative time interval for the study, which gave the opportunity to test model forecasts under reference conditions (high-pressure situations) and under some of the most problematic conditions to model (cold front, convergence line, etc.) [67,73,74].

Due to the nature of the analyzed parameter SWDDIR, the conducted research took into account synoptic situations that occurred during the day (synoptic maps for 12:00 developed by the Polish Institute of Meteorology and Water Management—National Research Institute (IMGW-PIB) [75] are presented in Figures 1 and A2–A4). Weather conditions on the first of the analyzed dates (17 July 2022) were associated with the eastern part of the wedge from the high-pressure system (1027 hPa) with a center over the northwestern part of Germany. There was subinversion cloudiness over the studied region, which was formed by stratiform clouds (St, Sc). On 18 July 2022, a cloud system was present over the region ahead of a wavy cold front associated with a filling low-pressure system, with its center located over the Norwegian Sea. On the following day (19 July 2022), the analyzed region was in an area of higher pressure, in a warm polar-maritime air mass, and free of cloud cover. On 20 July 2022, the analyzed area was located in the front area of the filling low-pressure system in the old tropical air mass, and the locally occurring cloudiness was determined via orography. The analyzed region, on 21 July 2022, was under the influence of the cloud system associated with the convergence line. Clouds of convective genesis were present. The area was in the range of a tropical air mass, with cooler polar-maritime air coming in from the west behind an incoming cool front. On the following day (22 July 2022), the region was affected by a wavy cold front associated with a filling low-pressure system with a center over the southern part of the Scandinavian Peninsula. Old tropical air masses were displaced by polar-maritime air masses. On 23 July 2022, the region was behind a wavy cold front, being in an area of higher atmospheric pressure associated with a high centered over the Bay of Biscay (1023 hPa) and a polar-maritime air mass. On that day, the cloud cover was mainly formed by clump clouds. Weather conditions on the last date were formed under the influence of an expanding high-pressure system, with a center over the Ore Mountains (1018 hPa), in a warm polar-maritime air mass. A summary of atmospheric conditions for the analyzed terms can be found below (Table 2).

NWP models, when forecasting atmospheric fronts, often inaccurately simulate the values of meteorological elements. Research conducted in [67] in the region of eastern Germany indicated that, especially in the case of cold fronts, the forecasts generated by the models have significant errors. An additional factor, which makes the forecast of meteorological conditions even more difficult, is the occurrence of a convergence line, which, together with its accompanying phenomena (convective clouds (Cumulonimbus)),

means that the models do not simulate properly [76–78]. For this reason, the situations associated with passing cold fronts (21–23 July 2022) were analyzed in detail.

Table 2. Atmospheric conditions prevailing in the region during the analyzed time interval (17–24 July 2022).

Date	Cloud Cover	Phenomena	Synoptic Situation
17 July 2022	Partial	Absence	High
18 July 2022	High	Absence	High
19 July 2022	Absence	Absence	High
20 July 2022	Absence/local	Absence	High
21 July 2022	High	Precipitation and convergence line	Cold front
22 July 2022	Absence	Absence	Cold front
23 July 2022	High	Precipitation	Cold front
24 July 2022	Absence	Absence	High

2.2. Parameterization of the WRF Model

The WRF ver. 4.3.3 model [79] was used for the study, and GFS input data with a spatial resolution of 0.25° and a temporal resolution of 3 h were applied [80]. A description of the domains can be found in Section 2.3.

The WRF model [81,82] was run in the following configuration: microphysics scheme—Thompson [83]; boundary layer represented by the Mellor–Yamada Nakanishi and Niino schemes [84,85]; shortwave radiation process parameterized via the Rapid Radiative Transfer Model for the general circulation models (RRTMG) scheme [86] (model configuration is consistent with WRF Solar settings [8,87]); surface layer—revised fifth-generation Pennsylvania State University–National Center for Atmospheric Research Mesoscale Model (MM5) scheme [88]; and land surface—Unified Noah Land Surface Model and shallow cumulus represented by the Deng scheme [35]. The parameterization of the WRF model used is shown below (Table 3).

Table 3. Weather Research and Forecasting Model (WRF) physics option configuration.

Model	Chosen Configuration
Vertical resolution	45 levels
Microphysics	Thompson Scheme
Planetary boundary layer	Mellor–Yamada Nakanishi Niino (MYNN)
Longwave radiation scheme	RRTMG
Shortwave radiation scheme	RRTMG
Land surface options	Unified Noah Land Surface Model
Shallow cumulus option	Deng Scheme
Surface layer options	Revised MM5 Scheme
Horizontal resolution	Depends on domain configuration (Table 4)

The WRF model was run for each day separately (in three varying variants, which took into account different domain configurations). Each time, a 12-hour spin-up time was adopted, meaning that the model could warm up properly—the forecast for a particular day was run the day before at 12:00 [89,90]. The time of day when direct radiation reached the Earth’s surface (from 3 a.m. to 7 p.m.) was used for subsequent analyses. A total of 24 simulations were carried out, with each simulation run (including spin-up time) for 36 h, with an output interval of 1 h.

Table 4. Characteristics of the WRF model domain configurations used in the study.

Domain Code	CR_3_2D ¹	CR_5_2D ²	CR_3_3D ³
Nesting ratio (grid parent ratio)	3	5	3
Number of domains	2	2	3
Domain spatial resolution 1	3 km	5 km	9 km
Domain spatial resolution 2	1 km	1 km	3 km
Domain spatial resolution 3	-	-	1 km
Dimensions of grids (number of nodes)	d01: 121 × 121 d02: 187 × 187	d01: 73 × 73 d02: 186 × 186	d01: 90 × 90 d02: 121 × 121 d03: 187 × 187

¹ two nested domains with grid parent ratios of 3; ² two nested domains with grid parent ratios of 5; ³ three nested domains with grid parent ratios of 3.

2.3. Domain Nesting Methods

The study compared the results of WRF model simulations performed on three different types of domains, using in each case one way nesting [91]. Two configurations were associated with two domains, while the third domain involved a three-domain configuration. Simulations with two domains, on the other hand, were performed for two different nesting ratios (grid parent ratio): 3 and 5. In the case of simulations with three domains, a grid parent ratio of 3 was used. In each of the above three-domain configurations, the smallest domain had a spatial resolution of about 1 km and covered the analyzed area (a square with a side of roughly 187 km and an area of roughly 35,000 km²); for each of them, the center of the domain had the same co-ordinates. The study focused only on the results of forecasts carried out for the domains with the highest spatial resolution. Table 4 summarizes the characteristics of the different domain configurations of the WRF model: a combination consisting of two nested domains with a grid parent ratio of 3—CR_3_2D, two-domain configurations with a nesting ratio of 5—CR_5_2D, and a three-domain combination with a ratio of 3—CR_3_3D.

In the following section of the article, the forecasts for the various configurations for the smallest domain are denoted by the main domain codes (CR_3_2D, CR_5_2D, or CR_3_3D).

3. Results

The results of the conducted studies have been analyzed through several aspects: the first compared the forecasts obtained for different domain configurations, the second confronted them with the data measured at the DWD stations, and the third compared the results of the WRF model forecasts made for a day (+24 h) or two days in advance (+48 h). In addition, for one of the dates (24 July 2022), the results of the simulations were compared with the data from observations and the direct components of radiation to the horizontal plane (theoretical) values.

Table 5 summarize general statistical characteristics (Pearson's coefficient, RMSE, MAE, MBE) on the results of simulations carried out for different domain configurations for the 24-h forecast.

It can be seen from the above tables that the Pearson's correlation coefficient takes similar values in each of the domain configurations (0.77 to 0.79 on average): in the case of the mean squared error, the configuration with three domains (CR_3_3D) is characterized by the smallest values, similar to the case of the value of the mean absolute error. The MBE analysis revealed that the CR_3_2D domain is characterized by the smallest values. The smallest error values and the highest correlation are achieved by the station located in

Leipzig. A more detailed analysis of the simulation results, taking into account the division into terms with high-pressure situations (cloudless conditions) and passing cold fronts, showed very good forecast results for the former conditions (Table 6).

Table 5. Statistical characteristics of 24-h forecast (Pearson’s [-], RMSE, MAE, MBE [$W \cdot m^{-2}$]).

	Pearson			RMSE			MAE			MBE		
	Dresden	Leipzig	Chemnitz									
CR_3_2D ¹ (24 h)	0.76	0.83	0.78	172.09	145.74	168.52	103.93	85.55	95.83	29.20	26.11	26.26
CR_5_2D ² (24 h)	0.74	0.79	0.78	182.64	163.10	169.60	110.21	93.38	93.48	31.63	26.10	33.43
CR_3_3D ³ (24 h)	0.77	0.78	0.79	172.78	165.23	164.06	101.42	91.45	93.84	37.88	21.83	23.44

¹ two nested domains with grid parent ratios of 3; ² two nested domains with grid parent ratios of 5; ³ three nested domains with grid parents ratio of 3.

Table 6. Summary of characteristics of the high-pressure situation (24-h forecast) (Pearson’s [-], RMSE, MAE, MBE [$W \cdot m^{-2}$]).

	Pearson			RMSE			MAE			MBE		
	Dresden	Leipzig	Chemnitz									
CR_3_2D ¹ (24 h)	0.94	0.95	0.96	96.23	89.45	90.54	68.48	56.98	59.19	-33.53	-27.77	-45.59
CR_5_2D ² (24 h)	0.94	0.93	0.97	97.28	100.24	82.15	68.62	61.98	54.21	-33.85	-32.82	-40.47
CR_3_3D ³ (24 h)	0.94	0.94	0.96	94.23	92.21	86.95	67.13	57.98	58.54	-29.44	-29.50	-43.26

¹ two nested domains with grid parent ratios of 3; ² two nested domains with grid parent ratios of 5; ³ three nested domains with grid parent ratios of 3.

Under high-pressure (reference) and cloudless conditions (Table 6), the value of the correlation coefficient ranged from 0.93 to 0.97, the values of the RMSE ranged from 86.95 to 100.24 [$W \cdot m^{-2}$], and the mean absolute error took values ranged from 54.21 to 68.62 [$W \cdot m^{-2}$], while the mean error for each of the configurations showed an underestimation relative to the observed data (from -45.59 to -27.77 [$W \cdot m^{-2}$]). The average MBE values for the first configuration were -35.63, for average values for the second were -35.71, and the average values for the third were -34.07 [$W \cdot m^{-2}$]. The best agreement is found by the Leipzig station (in the case of the correlation coefficient, it loses by 0.01 to the Chemnitz station).

In the above table (Table 7), the situations with a passing cold front are summarized, and a significant deterioration of the obtained results, relative to the observed data, is evident. Pearson’s correlation coefficient takes values from 0.32 to 0.60, and the mean square error ranges from 211.94 to 295.21 [$W \cdot m^{-2}$]. The mean absolute error takes values from 134.14 to 192.01 [$W \cdot m^{-2}$], while the mean error for each station and configuration takes positive values (from 80.54 to 184.29 [$W \cdot m^{-2}$]), which indicates an overestimation of the results obtained via the simulation. As in the case of the high-pressure situations, the Leipzig station performed best (in all parameters compared).

Table 7. Summary of characteristics for cold fronts (24-h forecast) (Pearson’s [-], RMSE, MAE, MBE [$W \cdot m^{-2}$]).

	Pearson			RMSE			MAE			MBE		
	Dresden	Leipzig	Chemnitz									
CR_3_2D ¹ (24 h)	0.40	0.60	0.35	254.47	211.94	282.57	168.46	134.14	182.71	140.78	100.42	164.51
CR_5_2D ² (24 h)	0.39	0.43	0.32	269.60	237.08	295.21	181.39	148.74	192.01	152.35	97.12	184.29
CR_3_3D ³ (24 h)	0.44	0.40	0.38	269.21	226.48	275.20	171.51	136.11	176.28	155.24	80.54	158.46

¹ two nested domains with grid parent ratios of 3; ² two nested domains with grid parent ratios of 5; ³ three nested domains with grid parent ratios of 3.

The study showed that the station located in the lowland (Leipzig) part of the region (the southwestern part of the Central German Lowland) had the best results (both in the aggregate and for high and cold front situations).

The best results were characterized by the CR_3_2D configuration—the effects of the comparison can be found in Table 8, which contains the values of statistical parameters relating to all data, which are determined for specific model configurations.

Table 8. Summary of results for each model configuration for 24-h forecasts (Pearson's, NSE [-], RMSE, MAE, MBE, nRMSE [$W \cdot m^{-2}$]).

	Pearson	RMSE	MAE	MBE	nRMSE	NSE
CR_3_2D ¹	0.79	162.12	95.10	27.19	0.69	0.57
CR_5_2D ²	0.77	171.78	99.03	30.39	0.73	0.51
CR_3_3D ³	0.78	167.36	95.57	27.71	0.71	0.54

¹ two nested domains with grid parent ratios of 3; ² two nested domains with grid parent ratios of 5; ³ three nested domains with grid parent ratios of 3.

In the case of predictions made for 24 h (Table 8), in fact, the simulation was run for 36 h (including a 12-h spin-up time), the three tested domain configurations gave similar results, although the CR_3_2D option performed slightly better, especially in terms of error values (primarily RMSE) (Table 8). The NSE coefficient values indicate that domains with grid parent ratios of 3 performed better than those with grid parent ratios of 5.

The smallest differences in the results of simulations performed for different domain configurations (Table 9) are characterized by the Dresden station (the correlation values are identical, while for RMSE, the difference between CR_3_2D and CR_3_3D is $1.02 [W \cdot m^{-2}]$, for MAE, it is below $3.5 [W \cdot m^{-2}]$, and for MBE, it is less than $3.3 [W \cdot m^{-2}]$ (Table 9)). Leipzig fared the worst in the above comparison.

Table 9. Statistical characteristics of the 48-h forecast (Pearson's [-], RMSE, MAE, MBE [$W \cdot m^{-2}$]).

	Pearson			RMSE			MAE			MBE		
	Dresden	Leipzig	Chemnitz									
CR_3_2D ¹ (48 h)	0.75	0.83	0.80	179.24	147.95	162.23	109.56	85.52	90.86	34.73	32.08	19.31
CR_5_2D ² (48 h)	0.75	0.80	0.79	178.75	158.52	169.40	108.84	90.77	95.12	32.37	30.01	28.30
CR_3_3D ³ (48 h)	0.75	0.78	0.80	178.22	166.62	162.99	106.11	92.31	94.88	31.46	31.76	23.80

¹ two nested domains with grid parent ratios of 3; ² two nested domains with grid parent ratios of 5; ³ three nested domains with grid parent ratios of 3.

In the case of days with high-pressure conditions accompanied by cloudless weather, the 48-h forecasts were characterized by high values of the correlation coefficient (Table 10)—for each of the domain configurations, identical values were obtained for individual stations (differences are visible in parts of thousands). Discrepancies in error values (RMSE, MAE) (Table 10) between configurations for individual stations are less than unity. Only in the case of MBE did they reach values up to and including $2.81 [W \cdot m^{-2}]$ (for the Chemnitz station).

Table 10. Summary of characteristics of the high-pressure situation (48-h forecast) (Pearson's [-], RMSE, MAE, MBE [$W \cdot m^{-2}$]).

	Pearson			RMSE			MAE			MBE		
	Dresden	Leipzig	Chemnitz									
CR_3_2D ¹ (48 h)	0.94	0.95	0.97	93.26	88.07	71.94	65.46	56.53	49.67	-22.50	-21.88	-30.50
CR_5_2D ² (48 h)	0.94	0.95	0.97	93.30	88.22	71.69	65.62	56.72	49.49	-22.81	-22.01	-30.15
CR_3_3D ³ (48 h)	0.94	0.95	0.97	93.34	89.03	71.31	65.20	57.21	49.24	-23.94	-22.96	-32.96

¹ two nested domains with grid parent ratios of 3; ² two nested domains with grid parent ratios of 5; ³ three nested domains with grid parent ratios of 3.

For situations associated with the passing of cold fronts, the differences between forecast results for different configurations of the computational domains and individual stations are much larger than for reference conditions (high-pressure situations) (Table 11). In the case of Pearson's correlation coefficient, the largest values were achieved for the Leipzig station (from 0.44 to 0.66), and the smallest values are achieved for the highest

located station of those compared—Chemnitz. The largest RMSE values characterized the Chemnitz and Dresden locations, similar to the other errors (MAE, MBE).

Table 11. Summary of characteristics for cold fronts (48-h forecast) (Pearson’s [-], RMSE, MAE, MBE [$W \cdot m^{-2}$]).

	Pearson			RMSE			MAE			MBE		
	Dresden	Leipzig	Chemnitz									
CR_3_2D ¹ (48 h)	0.38	0.66	0.20	273.29	198.70	275.82	185.58	125.26	174.92	157.36	110.84	136.54
CR_5_2D ² (48 h)	0.38	0.45	0.34	271.20	228.86	291.66	180.51	145.53	192.85	150.41	98.96	169.71
CR_3_3D ³ (48 h)	0.44	0.44	0.33	270.38	230.23	268.68	172.00	136.70	181.13	157.10	94.03	163.64

¹ two nested domains with grid parent ratios of 3; ² two nested domains with grid parent ratios of 5; ³ three nested domains with grid parent ratios of 3.

The summary above (Table 12) shows that the values of statistics obtained for simulations covering a 48-h time horizon are very similar to predictions run for 24 h. The differences between the values obtained for the respective model configurations are smaller for the longer forecasts than for the 24-h predictions. For 48-h simulations, better results were obtained than for 24-h simulations in high-pressure situations, the opposite happened for dates with passing cold fronts (especially for the Chemnitz station, where differences between Pearson’s coefficient values were as high as 0.15 for the same domain configuration). In the case of the NSE coefficient, all configurations take similar values; however, a slightly larger CR_3_2D was achieved. Below is a summary of the NSE coefficient for the domain configurations used for both 24-h and 48-h forecasts (Table 13).

Table 12. Summary of results for each model configuration for 48-h forecasts (Pearson’s, NSE [-], RMSE, MAE, MBE, nRMSE [$W \cdot m^{-2}$]).

	Pearson	RMSE	MAE	MBE	nRMSE	NSE
CR_3_2D ¹	0.79	163.14	95.32	28.71	0.70	0.56
CR_5_2D ²	0.78	168.89	98.24	30.22	0.72	0.53
CR_3_3D ³	0.78	169.28	97.77	29.01	0.72	0.53

¹ two nested domains with grid parent ratios of 3; ² two nested domains with grid parent ratios of 5; ³ three nested domains with grid parent ratios of 3.

Table 13. Summary of NSE coefficient values for different model configurations for 24- and 48-h forecasts.

	24 h			48 h		
	Dresden	Leipzig	Chemnitz	Dresden	Leipzig	Chemnitz
CR_3_2D ¹	0.48	0.62	0.59	0.52	0.63	0.55
CR_5_2D ²	0.48	0.56	0.55	0.46	0.54	0.55
CR_3_3D ³	0.48	0.52	0.58	0.51	0.53	0.58

¹ two nested domains with grid parent ratios of 3; ² two nested domains with grid parent ratios of 5; ³ three nested domains with grid parent ratios of 3.

The NSE coefficient (Table 13) assumed that the highest values (for both simulation times: 24 h and 48 h) for the Leipzig station, followed by the Chemnitz station and the Dresden station, was the worst in this respect. At the same time, clear differences between the NSE values become apparent, especially in the case of the Leipzig station, for the 24- and 48-h forecasts, with the discrepancies between the results of the different domain configurations bring 0.1. In each case, the high-pressure situations reached significantly better agreement than for the terms with cold fronts; for the 24-h simulations, the NSE took an average of 0.87 for Dresden, 0.87 for Leipzig, and 0.90 for Chemnitz. For the 48-h forecasts, the NSE coefficient determined for each station took slightly better agreement than for the 24-h forecast (Dresden: 0.88, Leipzig: 0.89, Chemnitz: 0.93). For dates with passing cold fronts, both for the 24- and 48-h forecasts and the NSE coefficient took negative values, indicating an insufficient prediction compared to observed mean. This issue was confirmed by the correspondingly lower values of Pearson’s coefficient; for 24-h simulations and days with cold fronts, it took values from 0.32 (Chemnitz) to 0.60 (Leipzig), while for

forecasts run for 48 h, the lowest value was reached by the station in Chemnitz (0.20), and the highest value (0.66) was achieved in Leipzig. For the selected date with a high-pressure situation (24 July 2022), the results of SWDDIR parameter simulations and observed data were compared with potential data (direct components of radiation to the horizontal plane) gathered from [72–74]. For each of the analyzed domain configurations, the potential values of direct radiation exceeded both simulated and measured values, especially during the midday hours (between 10 a.m. and 2 p.m.). The above comparison shows that the WRF model underestimates the amount of SWDDIR during the hours with the highest values of solar radiation delivery relative to the observed and potential data. Measured at DWD stations, the data are characterized by underestimation: on 24 July 2022, for Dresden, it averaged 72.0 $[\text{W}\cdot\text{m}^{-2}]$; for Leipzig, it averaged 79.7 $[\text{W}\cdot\text{m}^{-2}]$; and for Chemnitz, it averaged 93.1 $[\text{W}\cdot\text{m}^{-2}]$. In the case of WRF model simulation (CR_3_3D configuration), it took the following values: 145.6; 141.7, and 139.4 $[\text{W}\cdot\text{m}^{-2}]$, respectively (Figure 2). For the other two configurations, the discrepancies took on similar values; in this respect, the Chemnitz station stood out, at which the differences were slightly smaller than at the other stations, with the underestimation being below 140 $[\text{W}\cdot\text{m}^{-2}]$ (from 139.4 to 139.9 $[\text{W}\cdot\text{m}^{-2}]$).



Figure 2. The graphs show the daily distribution of modeled solar radiation (WRF) values, i.e., the measured and direct component of radiation to the horizontal plane (Direct component), for the analyzed stations on 24 July 2022: (a) Dresden, (b) Leipzig, and (c) Chemnitz. The lines of CR_3_2D, CR_5_2D, and CR_3_3D are overlapping (overlap each other). CR_3_2D: two nested domains with grid parent ratios of 3; CR_5_2D: two nested domains with grid parent ratios of 5; CR_3_3D: three nested domains with grid parent ratios of 3.

Below are graphs (Figure 3) showing the daily distribution of SWDDIR values at the Leipzig and Chemnitz stations, as well as maps (Figure 4) showing the spatial distribution of the analyzed solar parameters (for 15 and 16 h) for each of the three WRF model domain configurations for the 24-h simulation.

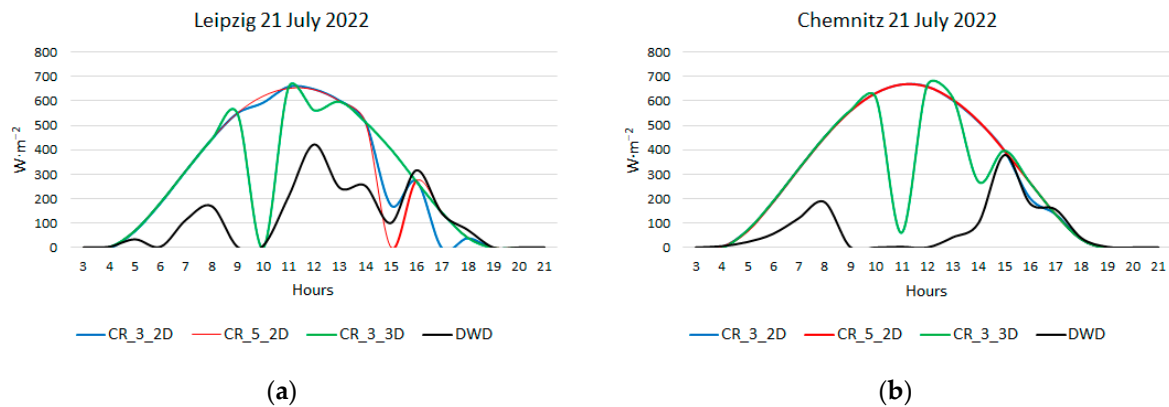


Figure 3. The graphs show the daily distribution of SWDDIR values for the Leipzig (a) and Chemnitz (b) stations on 21 July 2022. CR_3_2D: two nested domains with grid parent ratios of 3; CR_5_2D: two nested domains with grid parent ratios of 5; CR_3_3D: three nested domains with grid parent ratios of 3.

As an example, for the Leipzig station, the observation data for 3 p.m. shows a radiation sum of $100.00 \text{ [W}\cdot\text{m}^{-2}]$ (Figure 3), the model in the CR_3_3D configuration predicts a value of $403.52 \text{ [W}\cdot\text{m}^{-2}]$, CR_3_2D $175.43 \text{ [W}\cdot\text{m}^{-2}]$, and the two-domain combination of CR_5_2D is $0.17 \text{ [W}\cdot\text{m}^{-2}]$. Analysis of maps of spatial distribution of SWDDIR values shows that for the first two simulations, the Leipzig station was located at the border of the overcast zone—in this particular time interval, this fact determined the values that significantly exceeded the actual delivery of solar radiation (for domains with grid parent ratio 3), while for the last of the combinations, the station was under the cloud cover, which was reflected in the value being close to zero. The 4 p.m. data for the Chemnitz station, on the other hand, shows that the model simulated solar conditions very well, while, in this case, the measuring station was at the border of the modeled zone related to the presence of cloud cover (limited value of direct radiation reaching the Earth's surface) for the CR_3_2D and CR_5_2D configurations, although, in this situation, the simulated SWDDIR values differed from the measured ones only by about 5%.

The maps below (Figure 5) show the differences in the spatial distribution of SWDDIR parameter values between the different domain configurations for the date associated with the movement of the cold front (21 July 2022), i.e., when the greatest differences occurred. The dissimilarities occur both between the analyzed configurations and relative to the measured data. It is noticeable that there are greater values of differences between the two-domain configurations (CR_3_2D, CR_5_2D) and the three-domain combination (CR_3_3D). This result is especially evident in the southeastern part of the region (Ore Mountains Massif). The two-domain configurations are characterized by a marked similarity in the distribution of the SWDDIR parameter.

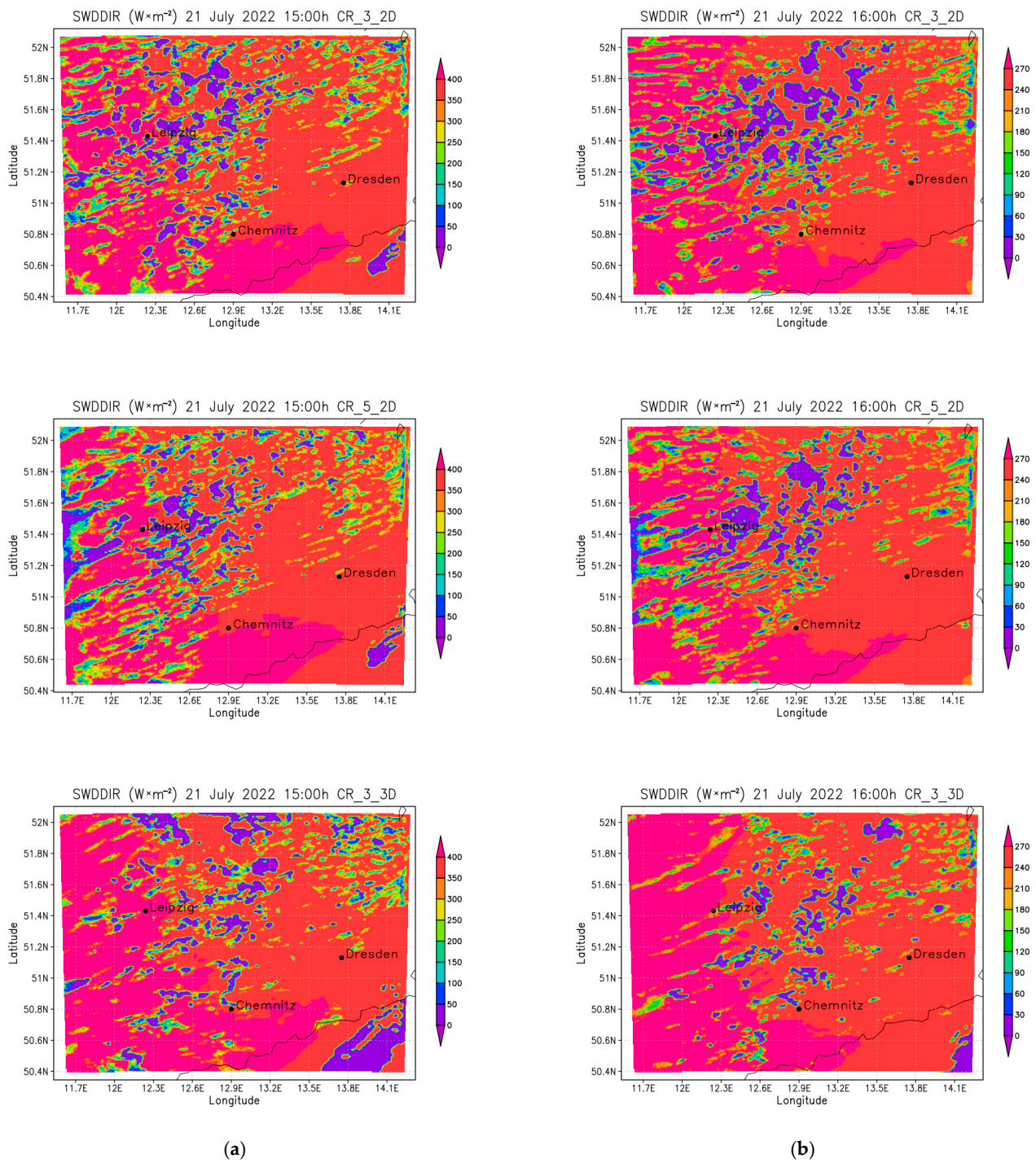


Figure 4. The maps show the spatial distribution of SWDDIR values for three domain configurations for 3 p.m. (a) and 4 p.m. (b) on 21 July 2022; CR_3_2D: two nested domains with a grid parent ratio of 3; CR_5_2D: two nested domains with a grid parent ratio of 5; CR_3_3D: three nested domains with a grid parent ratio of 3.

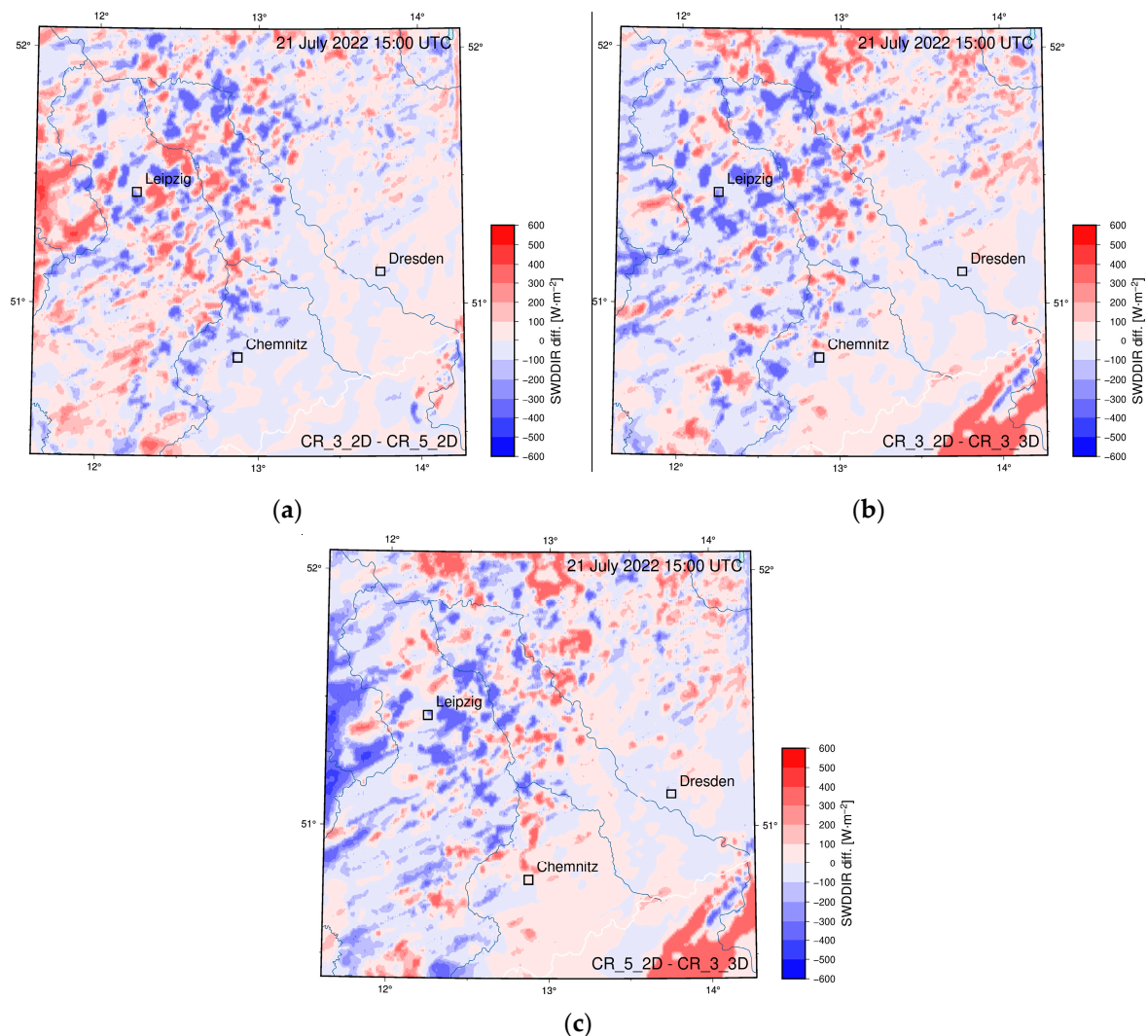


Figure 5. The maps show the differences in the spatial distribution of SWDDIR values between the analyzed domain configurations on 21 July 2022: ((a) CR_3_2D-CR_5_2D, (b) CR_3_2D-CR_3_3D, and (c) CR_5_2D-CR_3_3D). CR_3_2D: two nested domains with a grid parent ratio of 3; CR_5_2D: two nested domains with a grid parent ratio of 5; CR_3_3D: three nested domains with a grid parent ratio of 3.

A comparison between the values obtained from the WRF model simulations and the ERA5 analyses [92,93] showed that in the case of high pressure situations, the values from the WRF model are underestimated relative to ERA5. The differences took on smaller values for the forecasts made for two-domain combinations (CR_3_2D: -6.25 [$W \cdot m^{-2}$]; CR_5_2D: -6.02 [$W \cdot m^{-2}$]) than for three-domain configuration (CR_3_3D: -11.4 [$W \cdot m^{-2}$]). The situation was similar for median values (CR_3_3D: -14.62 [$W \cdot m^{-2}$]; CR_3_2D: -9.52 [$W \cdot m^{-2}$]; CR_5_2D: -9.28 [$W \cdot m^{-2}$]). For situations associated with a cold front, the values from the WRF model were overestimated. Here, the differences between the variants were already negligible, though they came out slightly better for the CR_3_2D configuration. The mean differences were 29.98, 28.57, and 28.90 [$W \cdot m^{-2}$] for the CR_3_3D, CR_5_2D, and CR_3_2D, respectively. Overall, the two-domain configurations were characterized by almost the same values. An example of differential maps for the term with a high-pressure situation (20 July 2022) and a moving cold front (22 July 2022) are shown below (Figure 6).

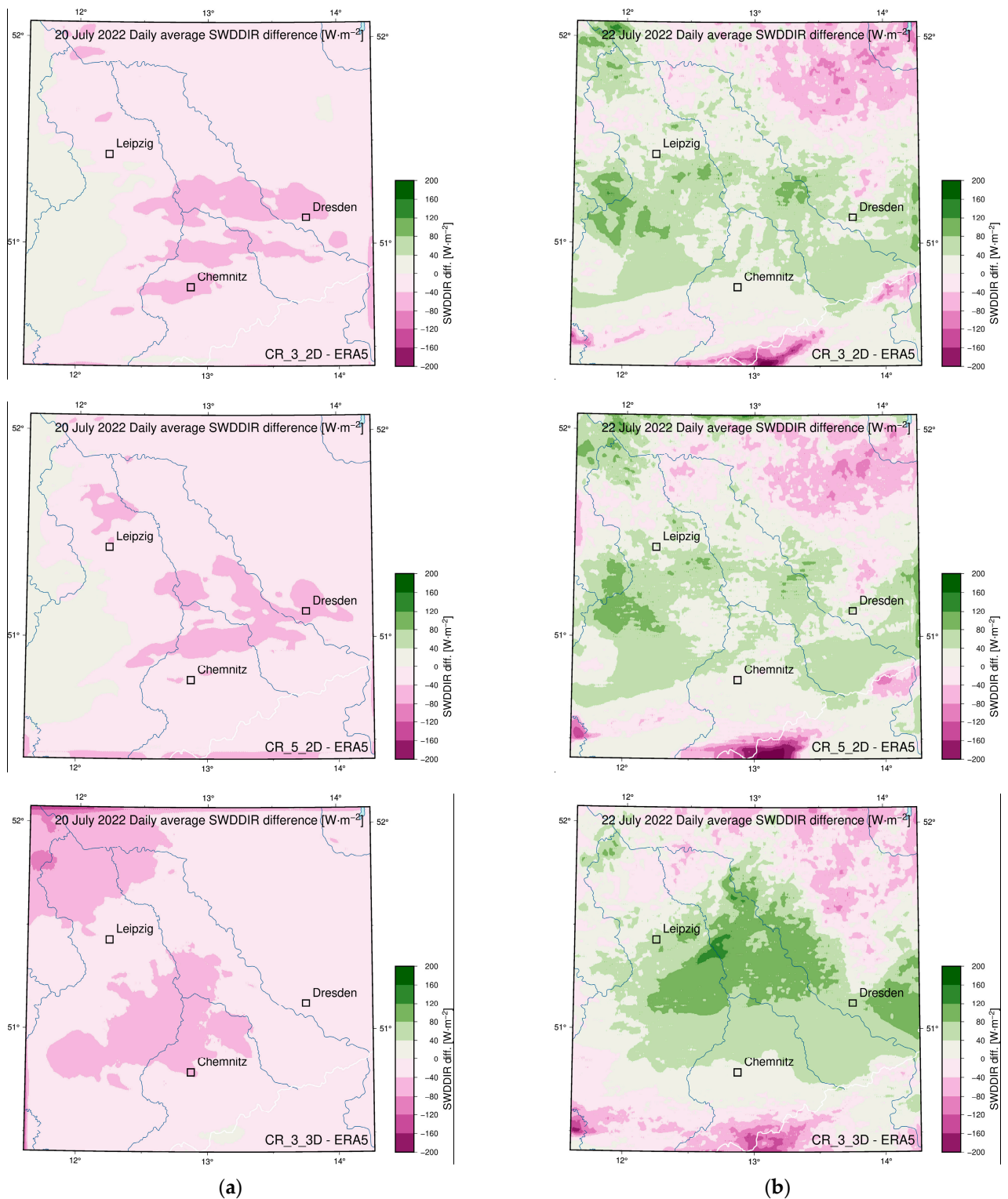


Figure 6. The difference maps of WRF model simulation results and ERA5 analyses for three domain configurations in two synoptic situations: a high (a) (20 July 2022) and a cold front (b) (22 July 2022); CR_3_2D: two nested domains with a grid parent ratio of 3; CR_5_2D: two nested domains with a grid parent ratio of 5; CR_3_3D: three nested domains with a grid parent ratio of 3.

4. Discussion

This study showed that the use of double nesting of domains produces results at the same quality level as produced for the use of triple nesting. This result indicates that choosing fewer domains achieves results in a faster and more efficient way (less output and temporary files are generated) than in the case of triple nesting. Carrying out predictions for a longer time horizon, i.e., covering 48 h in advance, obtained similar results—in the case of high-pressure situations, even better results were obtained than for 24-h predictions (Tables 6 and 10).

Due to the smaller number of nodes in the grid with a parent–grid ratio of 5 (CR_5_2D), the simulation time for this domain configuration is the shortest for simulations run for both 24 and 48 h (by an average of roughly 14% relative to the other 24-h values and by roughly 16% for the other 48-h forecasts). However, it is characterized by slightly worse results (analysis of correlation coefficients, errors) against other domain configurations, especially for the 24-h forecast (Table 8).

Differences between the results obtained for individual stations depend primarily on their location and the resulting different environmental conditions: relief, denivelations, height above sea level, land cover, etc. The use of shallow convection schemes (Deng scheme) [35], which were developed mainly for mesoscale weather forecast models, ensures proper simulation, especially of clouds of convective genesis (associated with cold fronts). Therefore, the application of domains with high spatial resolution (1 km) should not affect the results obtained.

The results of the model's forecasts are highly consistent with the observed data, especially during high (cloudless) situations—correlations (e.g., 24 July 2022) are, for each of the domain configurations, more than 0.99. The verifiability of forecasts is completely different for days with dynamically changing conditions, as during the movement of atmospheric fronts (e.g., 21 July 2022), the values of the correlation coefficient range from 0.37 to 0.48 (for the analyzed stations). The main purpose of this study was to examine the effect of the way domains are nested on the simulation results for the CEE area as a starting point for further research. Analysis of the results obtained for 24-h simulations showed a slight advantage of the CR_3_2D and CR_3_3D model configurations over CR_5_2D. Among the combinations of domains with parent–grid ratios of 3, the example with two domains (CR_3_2D) turned out to be more effective. The situation is analogous for simulations lasting 48 h. In the context of the analysis of synoptic situations (high-pressure systems, cold fronts), the above regularity also occurs.

The differences between the direct component of radiation to the horizontal plane and the directly measured or simulated planes are due to, among other things, the presence of aerosols, dust, etc., which can come from natural sources (floating dust, etc.) and anthropogenic sources (pollution, etc.) [70,71].

More detailed perturbation modeling experiments (enabling stochastic perturbation analysis for selected variables) that can be performed with the WRF-Solar Ensemble Prediction System (EPS) [94], which is currently available in beta version (it is still under development), will be the subject of further research. At that point, it will be possible to study in a more detailed way the sensitivity of the model to modifications of circumstantial variables, such as albedo or soil moisture. Work in this field is still being carried out. Different approaches are being used with the LES and WRF-Solar EPS models. Another prospect is the release of WRF-Solar V2 model, which the authors will include in their future research.

Table 14 shows a summary of Pearson's correlation coefficient values for data obtained via simulations conducted for all domain configurations for the date associated with the moving cold front (21 July 2022).

All configurations have the highest correlation coefficient values for the domains with the highest level of spatial resolution (1 km). Interestingly, there is the case of the three-domain configuration (CR_3_3D), in which the domain with lower spatial resolution (9 km) is characterized by greater similarity to the data created via direct measurements. In this case, the domain with a grid size of 3 km had 0.13 less correlation value than the 9 km domain and 0.20 less correlation than the 1 km domain. Similarly, Pearson's correlation values were compared for the date 24 July 2022, on which, due to the prevailing

atmospheric conditions (a high-pressure situation), the differences between the results (within a given configuration) were negligible.

Table 14. A summary of simulation results (Pearson’s coefficient [-]) for three domain configurations for the date 21 July 2022.

Domain Resolution	CR_3_2D ¹	CR_5_2D ²	CR_3_3D ³
1 km	0.38	0.37	0.48
3 km	0.27	-	0.28
5 km	-	0.30	-
9 km	-	-	0.41

¹ two nested domains with a grid parent ratio of 3; ² two nested domains with a grid parent ratio of 5; ³ three nested domains with a grid parent ratio of 3.

5. Conclusions

The present study indicated that in addition to the proper parameterization of the numerical weather forecast model (in this case, the Weather Research and Forecasting model), the simulation results were also affected by the selection of appropriate domains. The use of a model configuration consisting of three domains gives very similar results (slightly worse than a two-domain solution), while the duration of simulations is longer, and, thus, the performance is worse. It has been shown that:

- Analyses of different variants of domain nesting have shown that even with similar values of correlation coefficients (Pearson, NSE), error values can differ significantly.
- When analyzing synoptic situations, the highs were characterized by smaller differences in RMSE values for 24-h predictions (the maximum difference was 10.79 [W·m⁻²] for Leipzig) and even minimal differences for 48-h predictions (<1 [W·m⁻²] for each station).
- For spatially limited areas (as tested in the study), it would be better to use two domains with spatial resolutions of d01—3 km and d02—1 km than to perform simulations for three domains with grid sizes equal to the following figures: d01—9 km, d02—3 km, and d03—1 km.
- An in-depth analysis of the simulation results proved that forecasts covering 48 h were characterized by almost identical values of Pearson’s correlation coefficient (for the high-pressure situations and the overall stations), while the error values were smaller than those for the 24-h forecasts (for the Chemnitz station, the RMSE recorded values were smaller by up to 20.5% relative to the shorter simulation). The dates with cold fronts were characterized by smaller differences in RMSE values between simulations covering 24 and 48 h, which did not exceed 7%.

Finally, the study showed that for the analyzed region, the optimal solution—in the case of forecasting solar conditions using domains of high spatial resolution (1 km)—is the use of two domains, with a parent grid ratio of 3. Due to the scale of the analysis, it cannot be assumed that the proposed approach will be applicable across the entire globe.

Author Contributions: Conceptualization, M.M.; Methodology, M.M.; Validation, K.K.; Formal analysis, M.M.; Investigation, M.M.; Writing—original draft preparation, M.M.; Writing—review and editing, M.M. and K.K.; Visualization, M.M.; Supervision, K.K. All authors have read and agreed to the published version of the manuscript.

Funding: This research and the APC were funded by the Military University of Technology in Warsaw, the Faculty of Civil Engineering and Geodesy, the Institute of Geospatial Engineering, and the Geodesy statutory research funds UGB/22-816/2023/WAT.

Data Availability Statement: Not applicable.

Acknowledgments: The authors send special thanks to Andrzej Araszkiwicz for his assistance and consultation and Wojciech Trzeźniak for his contribution to the meteorological aspect. The authors acknowledge the DWD Climate Data Center (CDC) for providing the hourly station observation of solar incoming (total/diffuse) and longwave downward radiation for Germany. Numerical simulations were performed using Weather Research and Forecasting Model version 4.3.3 (<https://github.com/wrf-model/WRF/releases>, last accessed on 20 June 2023).

Conflicts of Interest: The authors declare no conflict of interest.

Appendix A

Table A1. List of abbreviations used in the entire article.

Abbreviation	Meaning
CEE	Central and Eastern Europe
DWD	Deutscher Wetterdienst
EU	European Union
GFS	Global Forecast System
IMGW-PIB	Polish Institute of Meteorology and Water Management—National Research Institute
LES	Large-eddy simulations
MAE	Mean absolute error
MBE	Mean bias error
MM5	Fifth-generation Pennsylvania State University-National Center for Atmospheric Research Mesoscale Model
nRMSE	Normalized root mean square error
NSE	Nash-Sutcliffe Efficiency
NWP	Numerical Weather Prediction
PV	Photovoltaic
RES	Renewable energy sources
RMSE	Root mean square error
RRTMG	Rapid Radiative Transfer Model for general circulation models
SWDDIR	Shortwave surface downward direct irradiance
UTC	Universal Time Coordinated
WRF	Weather Research and Forecasting Model
WRF-Solar EPS	WRF-Solar Ensemble Prediction System

Appendix B

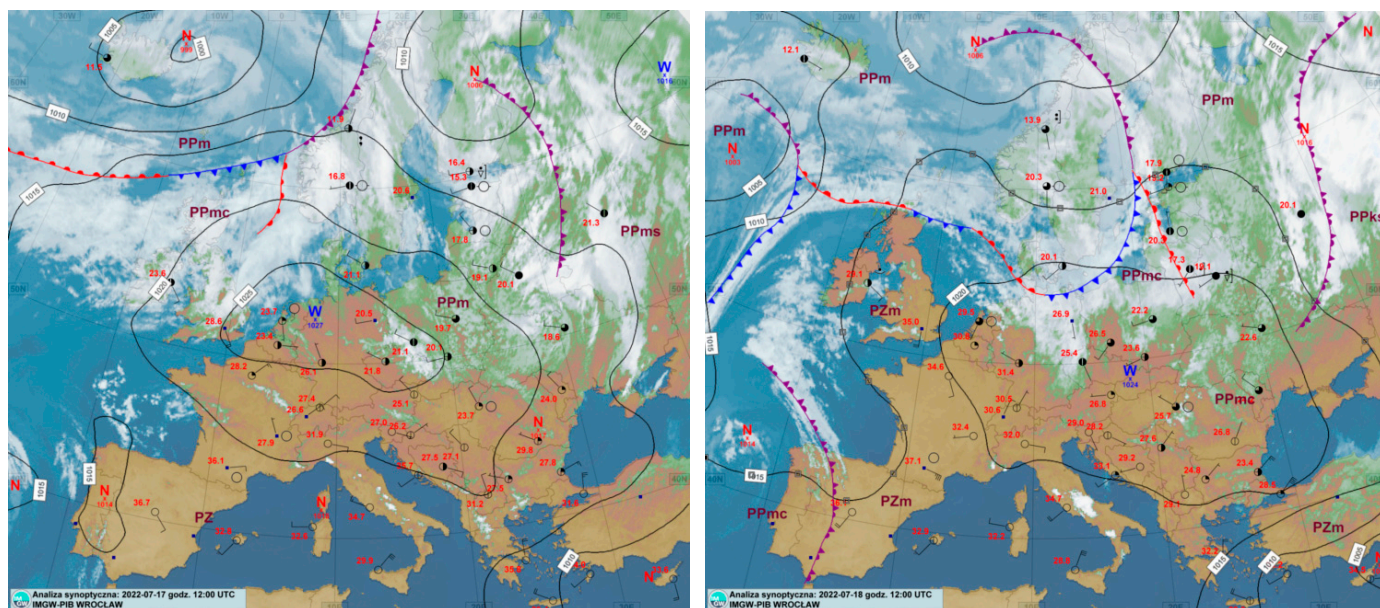


Figure A1. Synoptic map for 17 July 2022 at 12:00 [UTC] (on the left) and 18 July 2022 at 12:00 [UTC] (on the right).

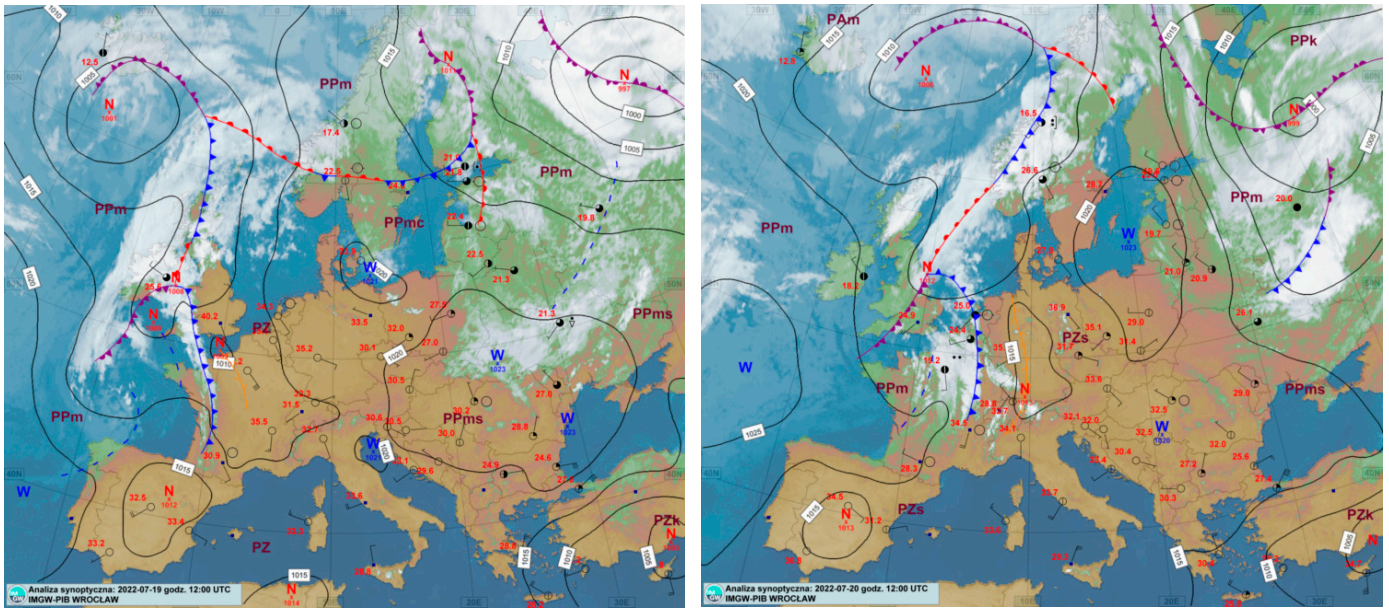


Figure A2. Synoptic map for 19 July 2022 at 12:00 [UTC] (on the left) and 20 July 2022 at 12:00 [UTC] (on the right).

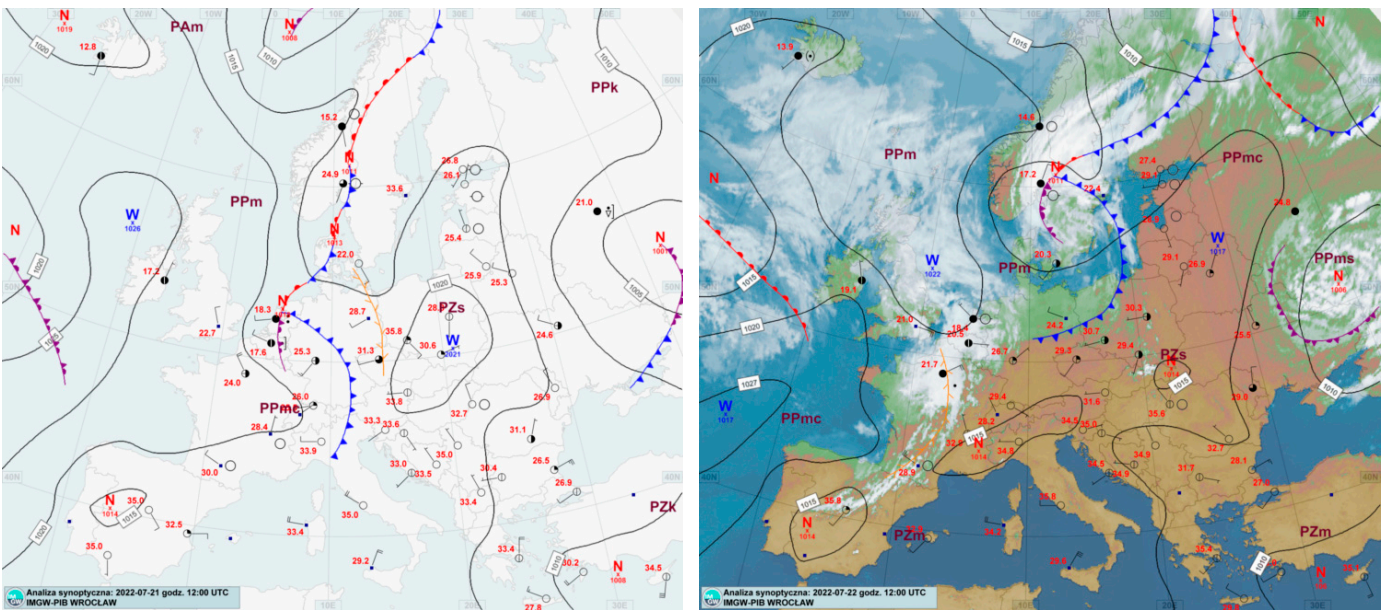


Figure A3. Synoptic map for 21 July 2022 at 12:00 [UTC] (on the left) and 22 July 2022 at 12:00 [UTC] (on the right).

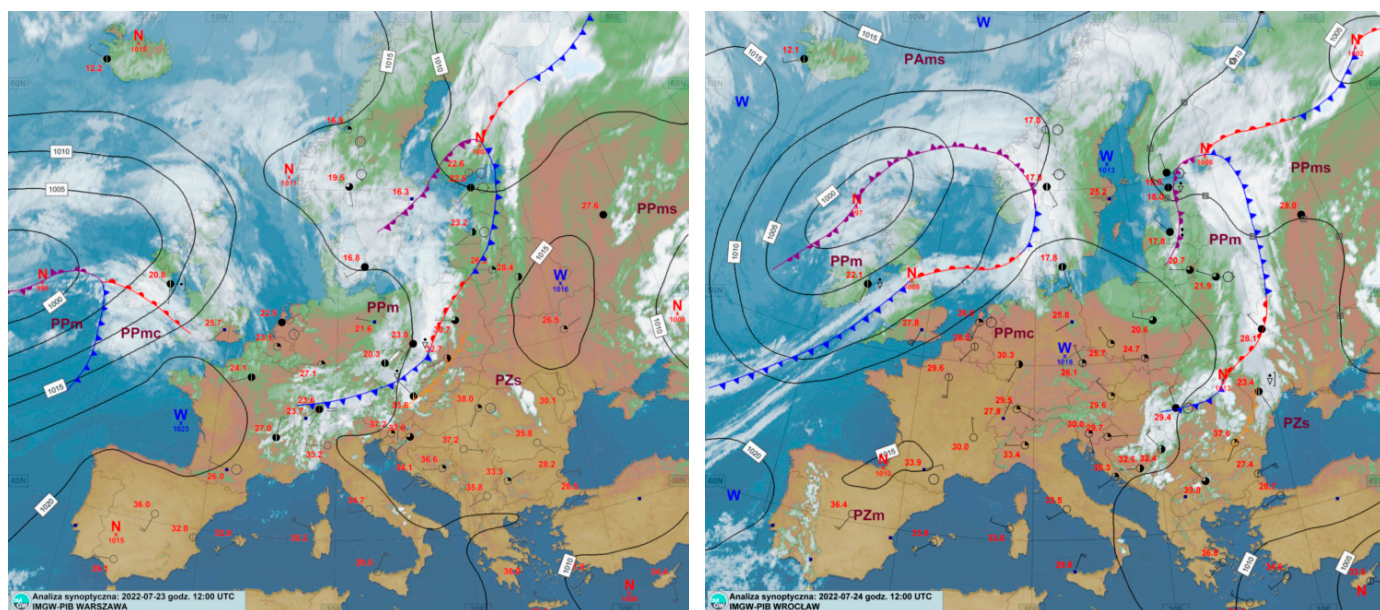


Figure A4. Synoptic map for 23 July 2022 at 12:00 [UTC] (on the left) and 24 July 2022 at 12:00 [UTC] (on the right).

References

1. In Focus: Renewable Energy in Europe. Available online: https://commission.europa.eu/news/focus-renewable-energy-europe-2020-03-18_en (accessed on 23 March 2023).
2. Technical Support for RES Policy Development and Implementation-Publications Office of the EU. Available online: <https://op.europa.eu/en/publication-detail/-/publication/6fcc38cb-1440-11ec-b4fe-01aa75ed71a1/language-en> (accessed on 23 March 2023).
3. Documenting a Decade of Cost Declines for PV Systems | News | NREL. Available online: <https://www.nrel.gov/news/program/2021/documenting-a-decade-of-cost-declines-for-pv-systems.html> (accessed on 23 March 2023).
4. Danner, P.; de Meer, H. Location and solar system parameter extraction from power measurement time series. *Energy Inform.* **2021**, *4*, 14. [CrossRef]
5. Kosmopoulos, P.G.; Kazadzis, S.; Lagouvardos, K.; Kotroni, V.; Bais, A. Solar energy prediction and verification using operational model forecasts and ground-based solar measurements. *Energy* **2015**, *93*, 1918–1930. [CrossRef]
6. Goh, H.H.; Li, C.; Zhang, D.; Dai, W.; Lim, C.S.; Kurniawan, T.A.; Goh, K.C. Application of choosing by advantages to determine the optimal site for solar power plants. *Sci. Rep.* **2022**, *12*, 4113. [CrossRef] [PubMed]
7. Fernandez-Jimenez, L.A.; Muñoz-Jimenez, A.; Falces, A.; Mendoza-Villena, M.; Garcia-Garrido, E.; Lara-Santillan, P.M.; Zorzano-Alba, E.; Zorzano-Santamaria, P.J. Short-term power forecasting system for photovoltaic plants. *Renew. Energy* **2012**, *44*, 311–317. [CrossRef]
8. Jimenez, P.A.; Hacker, J.P.; Dudhia, J.; Haupt, S.E.; Ruiz-Arias, J.A.; Gueymard, C.A.; Thompson, G.; Eidhammer, T.; Deng, A. WRF-SOLAR: Description and clear-sky assessment of an augmented NWP model for solar power prediction. *Bull. Am. Meteorol. Soc.* **2016**, *97*, 1249–1264. [CrossRef]
9. Žagar, N. A global perspective of the limits of prediction skill of NWP models. *New Pub Stock. Uni Press* **2017**, *69*, 1317573. [CrossRef]
10. Semmler, T.; Jung, T.; Kasper, M.A.; Serrar, S. Using NWP to assess the influence of the Arctic atmosphere on midlatitude weather and climate. *Adv. Atmos. Sci.* **2018**, *35*, 5–13. [CrossRef]
11. Wolniak, R.; Skotnicka-Zasadzień, B. Development of Photovoltaic Energy in EU Countries as an Alternative to Fossil Fuels. *Energies* **2022**, *15*, 662. [CrossRef]
12. EUR-Lex-32018L2001-EN-EUR-Lex. Available online: <https://eur-lex.europa.eu/legal-content/EN/TXT/?uri=CELEX:32018L2001> (accessed on 11 March 2023).
13. Communication from the Commission—Guidelines on State Aid for Environmental Protection and Energy 2014–2020. Available online: <https://eur-lex.europa.eu/legal-content/EN/TXT/?uri=CELEX%3A52014XC0628%2801%29> (accessed on 20 June 2023).
14. Status Review of Renewable Support Schemes in Europe for 2018 and 2019 CEER Report Renewables Work Stream of Electricity Working Group. 2021. Available online: <https://www.ceer.eu/documents/104400/-/-/ffe624d4-8fbb-ff3b-7b4b-1f637f42070a> (accessed on 20 June 2023).
15. EUR-Lex-l27067-EN-EUR-Lex. Available online: <https://eur-lex.europa.eu/EN/legal-content/summary/an-energy-policy-for-europe.html> (accessed on 11 March 2023).

16. Mitra, I.; Heinemann, D.; Ramanan, A.; Kaur, M.; Sharma, S.K.; Tripathy, S.K.; Roy, A. Short-term PV power forecasting in India: Recent developments and policy analysis. *Int. J. Energy Environ. Eng.* **2022**, *13*, 515–540. [CrossRef]
17. Orwig, K.D.; Ahlstrom, M.L.; Banunarayanan, V.; Sharp, J.; Wilczak, J.M.; Freedman, J.; Haupt, S.E.; Cline, J.; Bartholomy, O.; Hamann, H.F.; et al. Recent trends in variable generation forecasting and its value to the power system. *IEEE Trans. Sustain. Energy* **2015**, *6*, 924–933. [CrossRef]
18. Mathiesen, P.; Kleissl, J. Evaluation of numerical weather prediction for intra-day solar forecasting in the continental United States. *Sol. Energy* **2011**, *85*, 967–977. [CrossRef]
19. Kallio-Myers, V.; Riihelä, A.; Schoenach, D.; Gregow, E.; Carlund, T.; Anders, I.; Lindfors, V. Comparison of irradiance forecasts from operational NWP model and satellite-based estimates over Fennoscandia. *Meteorol. Appl.* **2022**, *29*, e2051. [CrossRef]
20. Perez, R.; Lorenz, E.; Pelland, S.; Beauharnois, M.; Van Knowe, G.; Hemker, K.; Heinemann, D.; Remund, J.; Müller, S.C.; Traunmüller, W.; et al. Comparison of numerical weather prediction solar irradiance forecasts in the US, Canada and Europe. *Sol. Energy* **2013**, *94*, 305–326. [CrossRef]
21. Short-Range Forecast-Glossary of Meteorology. Available online: https://glossary.ametsoc.org/wiki/Short-range_forecast (accessed on 28 February 2023).
22. Medium-Range Forecast-Glossary of Meteorology. Available online: https://glossary.ametsoc.org/wiki/Medium-range_forecast (accessed on 28 February 2023).
23. Frnda, J.; Durica, M.; Rozhon, J.; Vojtekova, M.; Nedoma, J.; Martinek, R. ECMWF short-term prediction accuracy improvement by deep learning. *Sci. Rep.* **2022**, *12*, 7898. [CrossRef]
24. Yáñez-Morróni, G.; Gironás, J.; Caneo, M.; Delgado, R.; Garreaud, R. Using the Weather Research and Forecasting (WRF) Model for Precipitation Forecasting in an Andean Region with Complex Topography. *Atmosphere* **2018**, *9*, 304. [CrossRef]
25. Siewert, J.; Kroszczynski, K. GIS data as a valuable source of information for increasing resolution of the WRF model for warsaw. *Remote Sens.* **2020**, *12*, 1881. [CrossRef]
26. Chang, H.I.; Kumar, A.; Niyogi, D.; Mohanty, U.C.; Chen, F.; Dudhia, J. The role of land surface processes on the mesoscale simulation of the July 26, 2005 heavy rain event over Mumbai, India. *Glob. Planet. Chang.* **2009**, *67*, 87–103. [CrossRef]
27. Xu, R.; Li, Y.; Teuling, A.J.; Zhao, L.; Spracklen, D.V.; Garcia-Carreras, L.; Meier, R.; Chen, L.; Zheng, Y.; Lin, H.; et al. Contrasting impacts of forests on cloud cover based on satellite observations. *Nat. Commun.* **2022**, *13*, 670. [CrossRef]
28. Steensen, B.M.; Marelle, L.; Hodnebrog, Myhre, G. Future urban heat island influence on precipitation. *Clim. Dyn.* **2022**, *58*, 3393–3403. [CrossRef]
29. Kautz, L.-A.; Martius, O.; Pfahl, S.; Pinto, J.G.; Ramos, A.M.; Sousa, P.M.; Woollings, T. Atmospheric blocking and weather extremes over the Euro-Atlantic sector—A review. *Weather Clim. Dynam.* **2022**, *3*, 305–336. [CrossRef]
30. Monteiro, M.J.; Couto, F.T.; Bernardino, M.; Cardoso, R.M.; Carvalho, D.; Martins, J.P.A.; Santos, J.A.; Argain, J.L.; Salgado, R. A Review on the Current Status of Numerical Weather Prediction in Portugal 2021: Surface–Atmosphere Interactions. *Atmosphere* **2022**, *13*, 1356. [CrossRef]
31. Dasari, H.P.; Salgado, R.; Perdigao, J.; Challa, V.S. A Regional Climate Simulation Study Using WRF-ARW Model over Europe and Evaluation for Extreme Temperature Weather Events. *Int. J. Atmos. Sci.* **2014**, *2014*, 704079. [CrossRef]
32. Beck, A.; Ahrens, B.; Staldbacher, K. Impact of nesting strategies in dynamical downscaling of reanalysis data. *Geophys. Res. Lett.* **2004**, *31*, 19101. [CrossRef]
33. Collins, S.N.; James, R.S.; Ray, P.; Chen, K.; Lassman, A.; Brownlee, J. Grids in Numerical Weather and Climate Models. In *Climate Change and Regional/Local Responses*; Chapter 4; InTech: Nord-Pas-de-Calais, France, 2013. [CrossRef]
34. Castorina, G.; Caccamo, M.T.; Insinga, V.; Magazù, S.; Munaò, G.; Ortega, C.; Semprebello, A.; Rizza, U. Impact of the Different Grid Resolutions of the WRF Model for the Forecasting of the Flood Event of 15 July 2020 in Palermo (Italy). *Atmosphere* **2022**, *13*, 1717. [CrossRef]
35. Deng, A.; Seaman, N.L.; Kain, J.S. A Shallow-Convection Parameterization for Mesoscale Models. Part I: Submodel Description and Preliminary Applications. *J. Atmos. Sci.* **2003**, *60*, 34–56. [CrossRef]
36. Implementation and Evaluation of a New Shallow Convection Scheme in WRF 26th Conference on Weather Analysis and Forecasting/22nd Conference on Numerical Weather Prediction, Atlanta, GA, Amer. Meteor. Soc., 12.5. Available online: <https://ams.confex.com/ams/94Annual/webprogram/Paper236925.html> (accessed on 9 May 2023).
37. Jeworrek, J.; West, G.; Stull, R. Evaluation of Cumulus and Microphysics Parameterizations in WRF across the Convective Gray Zone. *Weather Forecast.* **2019**, *34*, 1097–1115. [CrossRef]
38. Skamarock, W.C.; Klemp, J.B.; Dudhia, J.; Gill, D.O.; Liu, Z.; Berner, J.; Wang, W.; Powers, J.G.; Duda, M.G.; Barker, D.M.; et al. *A Description of the Advanced Research WRF Model Version 4.3*. 2021. Available online: <https://opensky.ucar.edu/islandora/object/opensky:2898> (accessed on 20 June 2023). [CrossRef]
39. Zhang, G.; Zhu, S.; Zhang, N.; Zhang, G.; Xu, Y. Downscaling Hourly Air Temperature of WRF Simulations Over Complex Topography: A Case Study of Chongli District in Hebei Province, China. *J. Geophys. Res. Atmos.* **2022**, *127*, e2021JD035542. [CrossRef]
40. Jang, S.; Lim, K.S.S.; Ko, J.; Kim, K.; Lee, G.; Cho, S.J.; Ahn, K.D.; Lee, Y.H. Revision of WDM7 Microphysics Scheme and Evaluation for Precipitating Convection over the Korean Peninsula. *Remote Sens.* **2021**, *13*, 3860. [CrossRef]
41. Umer, Y.; Ettema, J.; Jetten, V.; Steeneveld, G.J.; Ronda, R. Evaluation of the WRF Model to Simulate a High-Intensity Rainfall Event over Kampala, Uganda. *Water* **2021**, *13*, 873. [CrossRef]

42. Park, H.H.; Lee, J.; Chang, E.C.; Joh, M. High-Resolution Simulation of Snowfall over the Korean Eastern Coastal Region Using WRF Model: Sensitivity to Domain Nesting-Down Strategy. *Asia-Pac. J. Atmos. Sci.* **2019**, *55*, 493–506. [[CrossRef](#)]
43. Castorina, G.; Semprebello, A.; Insinga, V.; Italiano, F.; Caccamo, M.T.; Magazù, S.; Morichetti, M.; Rizza, U. Performance of the WRF Model for the Forecasting of the V-Shaped Storm Recorded on 11–12 November 2019 in the Eastern Sicily. *Atmosphere* **2023**, *14*, 390. [[CrossRef](#)]
44. Somses, S.; Bopape, M.J.M.; Ndarana, T.; Fridlind, A.; Matsui, T.; Phaduli, E.; Limbo, A.; Maikhudumu, S.; Maisha, R.; Rakate, E. Convection Parameterization and Multi-Nesting Dependence of a Heavy Rainfall Event over Namibia with Weather Research and Forecasting (WRF) Model. *Climate* **2020**, *8*, 112. [[CrossRef](#)]
45. Fierro, A.O.; Mansell, E.R.; Ziegler, C.L.; Macgorman, D.R. Application of a Lightning Data Assimilation Technique in the WRF-ARW Model at Cloud-Resolving Scales for the Tornado Outbreak of 24 May 2011. *Mon. Weather Rev.* **2012**, *140*, 2609–2627. [[CrossRef](#)]
46. Lee, J.A.; Haupt, S.E.; Jiménez, P.A.; Rogers, M.A.; Miller, S.D.; McCandless, T.C. Solar irradiance nowcasting case studies near sacramento. *J. Appl. Meteorol. Climatol.* **2017**, *56*, 85–108. [[CrossRef](#)]
47. Gueymard, C.; Jimenez, P. Validation of Real-Time Solar Irradiance Simulations Over Kuwait Using WRF-Solar. *ISES Conf. Proc.* **2019**, 1–11. [[CrossRef](#)]
48. Jee, J.B.; Kim, S. Sensitivity Study on High-Resolution WRF Precipitation Forecast for a Heavy Rainfall Event. *Atmosphere* **2017**, *8*, 96. [[CrossRef](#)]
49. Min, J.-S.; Roh, J.-W.; Jee, J.-B.; Kim, S. A Study on Sensitivity of Heavy Precipitation to Domain Size with a Regional Numerical Weather Prediction Model. *Atmosphere* **2016**, *26*, 85–95. [[CrossRef](#)]
50. Kotroni, V.; Lagouvardos, K. Evaluation of MM5 High-Resolution Real-Time Forecasts over the Urban Area of Athens, Greece. *J. Appl. Meteorol. Climatol.* **2004**, *43*, 1666–1678. [[CrossRef](#)]
51. Amirudin, A.A.; Salimun, E.; Zuhairi, M.; Tangang, F.; Juneng, L.; Mohd, M.S.F.; Chung, J.X. The Importance of Cumulus Parameterization and Resolution in Simulating Rainfall over Peninsular Malaysia. *Atmosphere* **2022**, *13*, 1557. [[CrossRef](#)]
52. DWD Climate Data Center (CDC): Hourly Station Observations of Solar Incoming (Total/Diffuse) and Longwave Downward Radiation for Germany, Version Recent. Available online: https://opendata.dwd.de/climate_environment/CDC/observations_germany/climate/hourly/solar/DESCRIPTION_obsgermany_climate_hourly_solar_en.pdf (accessed on 16 June 2023).
53. Zhong, X.; Dutta, U. Engaging Nash-Sutcliffe Efficiency and Model Efficiency Factor Indicators in Selecting and Validating Effective Light Rail System Operation and Maintenance Cost Models. *J. Traffic Transp. Eng.* **2015**, *3*, 255–265. [[CrossRef](#)]
54. Zeybek, M. Nash-Sutcliffe Efficiency Approach For Quality Improvement. *J. Appl. Math. Comput.* **2018**, *2*, 496–503. [[CrossRef](#)]
55. Kim, J.Y.; Yun, C.Y.; Kim, C.K.; Kang, Y.H.; Kim, H.G.; Lee, S.N.; Kim, S.Y. Evaluation of WRF model-derived direct irradiance for solar thermal resource assessment over South Korea. *AIP Conf. Proc.* **2017**, *1850*, 140013. [[CrossRef](#)]
56. Schemm, S.; Sprenger, M.; Martius, O.; Wernli, H.; Zimmer, M.; Schemm, S.; Sprenger, M.; Martius, O.; Wernli, H.; Zimmer, M. Increase in the number of extremely strong fronts over Europe? A study based on ERA-Interim reanalysis (1979–2014). *GeoRL* **2017**, *44*, 553–561. [[CrossRef](#)]
57. Ramirez-Vergara, J.; Bosman, L.B.; Leon-Salas, W.D.; Wollega, E. Ambient temperature and solar irradiance forecasting prediction horizon sensitivity analysis. *Mach. Learn. Appl.* **2021**, *6*, 100128. [[CrossRef](#)]
58. Chai, T.; Draxler, R.R. Root mean square error (RMSE) or mean absolute error (MAE)?-Arguments against avoiding RMSE in the literature. *Geosci. Model Dev.* **2014**, *7*, 1247–1250. [[CrossRef](#)]
59. Willmott, C.J.; Matsuura, K. Advantages of the mean absolute error (MAE) over the root mean square error (RMSE) in assessing average model performance. *Clim. Res.* **2005**, *30*, 79–82. [[CrossRef](#)]
60. Werner, K. NESTING IN WRF. 2019. Available online: http://140.112.69.65/research/coawst/COAWST_TUTORIAL/training_2019/monday/werner_nesting.pdf (accessed on 20 June 2023).
61. Wang, W.; Gill, D. WRF Nesting. 2012. Available online: https://ruc.noaa.gov/wrf/wrf-chem/wrf_tutorial_2012_brazil/WRF_nesting.pdf (accessed on 20 June 2023).
62. Schumacher, V.; Fernández, A.; Justino, F.; Comin, A. WRF High Resolution Dynamical Downscaling of Precipitation for the Central Andes of Chile and Argentina. *Front. Earth Sci.* **2020**, *8*, 328. [[CrossRef](#)]
63. WRF Users' Guide. Available online: https://www2.mmm.ucar.edu/wrf/users/docs/user_guide_v4/v4.4/contents.html (accessed on 22 November 2022).
64. Li, X.; Fan, K.; Yu, E. A Heavy Rainfall Event in Autumn over Beijing—Atmospheric Circulation Background and Hindcast Simulation Using WRF. *J. Meteorol. Res.* **2018**, *32*, 503–515. [[CrossRef](#)]
65. Zhu, K.; Xue, M. 1240-1258 China for an extreme rainfall event on 21 July 2012 in Beijing. *Adv. Atmos. Sci.* **2016**, *33*, 1240–1258. [[CrossRef](#)]
66. Pieri, A.B.; von Hardenberg, J.; Parodi, A.; Provenzale, A. Sensitivity of Precipitation Statistics to Resolution, Microphysics, and Convective Parameterization: A Case Study with the High-Resolution WRF Climate Model over Europe. *J. Hydrometeorol.* **2015**, *16*, 1857–1872. [[CrossRef](#)]
67. Mierzwia, M.; Kroszczyński, K.; Araszkiwicz, A. On Solar Radiation Prediction for the East-Central European Region. *Energies* **2022**, *15*, 3153. [[CrossRef](#)]
68. Gula, J.; Peltier, W.R. Dynamical Downscaling over the Great Lakes Basin of North America Using the WRF Regional Climate Model: The Impact of the Great Lakes System on Regional Greenhouse Warming. *J. Clim.* **2012**, *25*, 7723–7742. [[CrossRef](#)]

69. Garnier, B.J.; Ohmura, A. A method of calculating the direct shortwave radiation income of slopes. *J. Appl. Meteorol.* **1968**, *7*, 796–800. [CrossRef]
70. W.M.O. *Compendium of Lectures Notes in Climatology for Class III and Class IV Personnel*; W.M.O.: Geneva, Switzerland, 1992; ISBN 978-92-63-10726-8.
71. Chapter 4 Estimation of Solar Radiation | The MeteoLand Reference Book. Available online: <https://emf-creaf.github.io/meteolandbook/solarradiation.html> (accessed on 16 May 2023).
72. Total solar Irradiance-Glossary of Meteorology. Available online: https://glossary.ametsoc.org/wiki/Total_solar_irradiance (accessed on 14 June 2023).
73. Lamraoui, F.; Booth, J.F.; Naud, C.M. WRF Hindcasts of Cold Front Passages over the ARM Eastern North Atlantic Site: A Sensitivity Study. *Mon. Weather Rev.* **2018**, *146*, 2417–2432. [CrossRef]
74. Vijverberg, S.; Schmeits, M.; van der Wiel, K.; Coumou, D. NWP and Radar Extrapolation: Comparisons and Explanation of Errors. *Mon. Weather Rev.* **2020**, *148*, 4783–4798. [CrossRef]
75. Dane Publiczne. Available online: <https://danepubliczne.imgw.pl/datastore> (accessed on 15 October 2022).
76. Convergence Line-Glossary of Meteorology. Available online: https://glossary.ametsoc.org/wiki/Convergence_line (accessed on 15 November 2022).
77. Convergence Lines-Met Office. Available online: <https://www.metoffice.gov.uk/weather/learn-about/weather/types-of-weather/clouds/other-clouds/convergence-lines> (accessed on 15 November 2022).
78. Gevorgyan, A. Convection-Permitting Simulation of a Heavy Rainfall Event in Armenia Using the WRF Model. *Atmospheres* **2018**, *123*, 11008–11029. [CrossRef]
79. Release WRF Version 4.3.3 (Bug-fix Release) wrf-Model/WRF GitHub. Available online: <https://github.com/wrf-model/WRF/releases/tag/v4.3.3> (accessed on 27 March 2023).
80. National Centers for Environmental Prediction/National Weather Service/NOAA/U.S. Department of Commerce. 2015, updated daily. NCEP GFS 0.25 Degree Global Forecast Grids Historical Archive. Research Data Archive at the National Center for Atmospheric Res. Available online: <https://rda.ucar.edu/datasets/ds084.1/> (accessed on 20 June 2023).
81. Powers, J.G.; Klemp, J.B.; Skamarock, W.C.; Davis, C.A.; Dudhia, J.; Gill, D.O.; Coen, J.L.; Gochis, D.J.; Ahmadov, R.; Peckham, S.E.; et al. The Weather Research and Forecasting Model: Overview, System Efforts, and Future Directions. *Bull. Am. Meteorol. Soc.* **2017**, *98*, 1717–1737. [CrossRef]
82. Skamarock, W.C.; Klemp, J.B. A time-split nonhydrostatic atmospheric model for weather research and forecasting applications. *J. Comput. Phys.* **2008**, *227*, 3465–3485. [CrossRef]
83. Thompson, G.; Field, P.R.; Rasmussen, R.M.; Hall, W.D. Explicit Forecasts of Winter Precipitation Using an Improved Bulk Microphysics Scheme. Part II: Implementation of a New Snow Parameterization. *Mon. Weather Rev.* **2008**, *136*, 5095–5115. [CrossRef]
84. Nakanishi, M.; Niino, H. An improved Mellor-Yamada Level-3 model: Its numerical stability and application to a regional prediction of advection fog. *Bound. Layer Meteorol.* **2006**, *119*, 397–407. [CrossRef]
85. Nakanishi, M.; Niino, H. Development of an Improved Turbulence Closure Model for the Atmospheric Boundary Layer. *J. Meteorol. Soc. Japan. Ser. II* **2009**, *87*, 895–912. [CrossRef]
86. Iacono, M.J.; Delamere, J.S.; Mlawer, E.J.; Shephard, M.W.; Clough, S.A.; Collins, W.D. Radiative forcing by long-lived greenhouse gases: Calculations with the AER radiative transfer models. *J. Geophys. Res. Atmos.* **2008**, *113*, 13103. [CrossRef]
87. Ruiz-Arias, J.A.; Dudhia, J. A simple parameterization of the short-wave aerosol optical properties for surface direct and diffuse irradiances assessment in a numerical weather model. *Geosci. Model Dev.* **2014**, *7*, 593–629. [CrossRef]
88. Jiménez, P.A.; Dudhia, J.; González-Rouco, J.F.; Navarro, J.; Montávez, J.P.; García-Bustamante, E. A Revised Scheme for the WRF Surface Layer Formulation. *Mon. Weather Rev.* **2012**, *140*, 898–918. [CrossRef]
89. Short, C.J.; Petch, J. Reducing the spin-up of a regional NWP system without data assimilation. *Q. J. R. Meteorol. Soc.* **2022**, *148*, 1623–1643. [CrossRef]
90. Bonekamp, P.N.J.; Collier, E.; Immerzeel, W. The Impact of Spatial Resolution, Land Use, and Spinup Time on Resolving Spatial Precipitation Patterns in the Himalayas. *J. Hydrometeorol.* **2018**, *19*, 1565–1581. [CrossRef]
91. WRF-Solar. Available online: <https://ral.ucar.edu/documentation/wrf-solar-reference-configuration> (accessed on 20 June 2023).
92. Hersbach, H.; Bell, B.; Berrisford, P.; Hirahara, S.; Horányi, A.; Muñoz-Sabater, J.; Nicolas, J.; Peubey, C.; Radu, R.; Schepers, D.; et al. The ERA5 global reanalysis. *Q. J. R. Meteorol. Soc.* **2020**, *146*, 1999–2049. [CrossRef]
93. Radiation Quantities in the ECMWF Model and MARS. Available online: <https://www.ecmwf.int/en/elibrary/18490-radiationquantities-ecmwf-model-and-mars> (accessed on 16 June 2023).
94. WRF-Solar®EPS | Research Applications Laboratory. Available online: <https://ral.ucar.edu/solutions/products/wrf-solar-eps> (accessed on 18 April 2023).

Disclaimer/Publisher’s Note: The statements, opinions and data contained in all publications are solely those of the individual author(s) and contributor(s) and not of MDPI and/or the editor(s). MDPI and/or the editor(s) disclaim responsibility for any injury to people or property resulting from any ideas, methods, instructions or products referred to in the content.